Supersonic Airfoil Optimization

James L. Pittman*
NASA Langley Research Center, Hampton, Virginia

A procedure for the optimization of supersonic airfoils is presented. A nonlinear, full-potential solver (NCOREL) is coupled with a numerical optimizer (CONMIN). The NCOREL code is a three-dimensional supersonic marching method; however, only two-dimensional (conical) results are used for the airfoil problem. Each airfoil evaluated in the NCOREL aerodynamic code is composed of a linear combination of user-specified basis airfoils. The weighting factors of the basis airfoils plus the angle of attack form the design variable vector. The inviscid drag coefficient is minimized subject to lift and crossflow Mach number gradient constraints. The optimization strategy is found to be extremely important for the efficient determination of an optimum airfoil.

Nomenclature

a	= speed of sound, Eqs. (1) and (2)
a_i	= basis airfoil weighting factors, Eq. (8)
a_0	= stagnation speed of sound, Eq. (2)
C_{D_i}	= inviscid drag coefficient
C_L	= calculated lift coefficient, Eqs. (5) and (6)
$C_{L_{\text{design}}}$	= user-specified lower lift coefficient, Eq. (5)
$C_{L_{\text{up}}}$	= user-specified upper lift coefficient, Eq. (6)
C_p	= surface pressure coefficient
F	= general objective function, Eq. (3)
G_j	= general inequality constraints, Eq. (4)
I	= leading-edge radius parameter (Fig. 2, Table 1) or grid point identifier, Eq. (7)
i, j, m, n	= dummy indices, Eqs. (4) and (8)
M	= freestream Mach number
M_c	= crossflow Mach number
n	= number of basis airfoils
$\bar{Q}$	= total velocity vector, Eqs. (1) and (2)
$\bar{X}$	= design variable vector, Eqs. (3) and (4)
$\bar{Y}$	= composite airfoil, Eq. (8)
Y'	= basis airfoil, Eq. (8)
Y_{LE}	= local spanwise location of wing leading edge
z	= global vertical coordinate
α	= angle of attack, deg
α_i	= initial angle of attack, deg
γ	= ratio of specific heats
θ	= wing tip camber angle, see. Fig. 2
η	= nondimensional spanwise coordinate
Λ_{LE}	= leading-edge-sweep angle

Introduction

ENGINEERING work naturally involves optimization, i.e., the "best" set of design parameters that will satisfy a given set of constraints. Often, this work is accomplished by the laborious and time-consuming approach of extensive trade studies. A more efficient approach is to allow an optimization algorithm to make decisions to move the design toward the optimum in an automated fashion. One engineering problem that has been approached with automated optimizers is aerodynamic design. As computational speeds increase and as more efficient and reliable computational algorithms are developed, the approach that couples aerodynamic analysis tools with automated optimizers becomes more practical. Overviews of aerodynamic optimization can be found in Refs. 1 and 2. Since the publication of Refs. 1 and 2, several additional papers have been published on the topic of transonic aerodynamic optimization.[3-7] Previous work for supersonic flow has utilized linear aerodynamic methods that are amenable to direct optimization for infinitely thin camber surfaces for three-dimensional wings.[8-10] Experimental verification of the supersonic linear theory optimum design, however, has achieved less than 50% of the theoretically predicted gains.[11] Problems arise from the weaknesses in the linear aerodynamic method, which decouples thickness from camber and which has a singularity at the leading edge of a wing swept within the freestream Mach cone (subsonic leading edge). Consequently, a need exists for a more accurate method of defining optimum wings in supersonic flow. An initial step in the development of this capability is the investigation of the two-dimensional problem.

The present study describes a method that couples a nonlinear, full-potential code (NCOREL)[12,13] for supersonic flow with an automated optimization code (CONMIN).[14] The NCOREL nonlinear, full-potential code couples thickness, camber, and angle-of-attack effects by solving exact tangential flow boundary conditions on the wing surface. The leading-edge singularity present in linearized potential theory is not present in the nonlinear potential theory. Consequently, accurate surface pressures are computed on the actual wing surface including the leading edge. Also, the position and strength of the bow shock, as well as the occurrence of embedded flowfield shocks, are accurately computed for low-to-moderate supersonic Mach numbers.

The CONMIN optimization program is a gradient search method that was chosen for reliability and robustness. Due to its widespread use for engineering problems, the original code has been updated several times, yielding a more mature and reliable technique.

Nonlinear, Full-Potential Aerodynamic Method

The NCOREL code solves the nonconservative form of the steady-flow, three-dimensional, full-potential equation written in spherical coordinates. The governing equations in terms of the velocity vector $\bar{Q}$ and the speed of sound a may be written

Presented as Paper 86-1818 at the AIAA 4th Applied Aerodynamics, San Diego, CA, June 9–11, 1986; received Oct. 22, 1986; revision received April 13, 1987.

*Aerospace Technologist, Fundamental Aerodynamics Branch, High-Speed Aerodynamics Division. Associate Fellow AIAA.

as

$$a^2\nabla \cdot \bar{Q} - \tfrac{1}{2}\bar{Q} \cdot \nabla(\bar{Q} \cdot \bar{Q}) = 0 \tag{1}$$

and

$$a^2 + [(\gamma - 1)/2]\bar{Q} \cdot \bar{Q} = a_0^2 \tag{2}$$

Exact boundary conditions are specified on the body surface. The three-dimensional full-potential equation written in a spherical coordinate system reduces identically to the conical (two-dimensional), full-potential equation in the initial data plane. The conical equation is used to initiate the three-dimensional marching solution, which then marches implicitly in space along concentric spheres at user-specified radii. Implicit marching was chosen since this method allows larger step sizes than is possible with explicit marchers. For the present application, however, only the conical (two-dimensional) results are required; therefore, no space marching is performed.

Grid generation is controlled by specifying marching step size and the number of grid points for each spherical solution plane. The grid points in each spherical solution plane are evenly spaced in the radial direction between the inner boundary (the geometry) and the outer boundary (the bow shock). The grid points around the geometry are clustered in a cosine fashion at the leading edge since this is the region of large flow gradients. The resulting set of linear, simultaneous equations is solved using the successive line over relaxation (SLOR)[12] or the approximate factorization (AFIZ)[15] technique. The other aspects of grid generation and mapping are internal to the code.

The sketch in Fig. 1 shows a delta-wing planform and two airfoil sections of the planform. Section A–A is a typical airfoil section for subsonic and transonic analysis and design. Due to the different physics of the supersonic flow, however, a more physically meaningful airfoil for supersonic Mach numbers is section B–B. This section is the intersection of the two-dimensional spherical surface, which is a sphere centered at the apex of the planform, with the wing planform. Therefore, a supersonic airfoil can also be considered a semi-infinite cone of arbitrary cross section. The optimization procedure will consider only zero sideslip; consequently, only half the supersonic airfoil will be analyzed.

Optimization Method

The CONMIN code iteratively solves linear or nonlinear constrained optimization problems using the conjugate gradient method[16] or the method of feasible directions.[17,18] Given a set of initial conditions for the design variables and a set of design constants, the code first determines if the initial values are in the feasible design space, i.e., the space where none of the design constraints are violated. If not, then the design variables must be changed until the feasible design space is located. At this point, the method can search to find the optimum design within the feasible design space. For the present study, the CONMIN code is used, so that for each of the n design variables, the analysis code is called for each perturbation of the design variables. The information from the analysis code is used in CONMIN to determine the direction and magnitude of the move in the n-dimensional design space.

Optimization Problem

The optimization problem is stated mathematically as

$$\text{Minimize } F(\bar{X}) \tag{3}$$

$$\text{subject to } G_j(\bar{X}) \le 0, \qquad j = 1, m \tag{4}$$

where F is the objective function, G_j are the inequality constraints, and $\bar{X}$ is a vector of design variables determined by the optimizer. For the supersonic airfoil problem, the objective function is the inviscid drag coefficient C_{D_i}, and the constraints are

$$1 - \frac{C_L}{C_{L_{\text{design}}}} \le 0 \tag{5}$$

$$\frac{C_L}{C_{L_{\text{up}}}} - 1 \le 0 \tag{6}$$

and

$$M_c(I) - M_c(I+1) - \Delta M_c \le 0 \tag{7}$$

where $C_{L_{\text{design}}}$ and $C_{L_{\text{up}}}$ are specified by the user. The desired final lift coefficient is $C_{L_{\text{design}}}$, and $C_{L_{\text{up}}}$ is an upper limit. The upper lift coefficient constraint is not necessary to work the problem since an optimization of inviscid drag coefficient drives the lift coefficient to lower values, but the upper constraint provides a more efficient search if the initial analysis yielded a lift coefficient well above $C_{L_{\text{design}}}$.

Equation (7) is a constraint on crossflow Mach number gradient and is intended to be an empirical means of preventing flow separation, which is linked to strong flow gradients. A sudden drop in crossflow Mach number from the point I to point $I+1$ indicates an embedded shock in the flowfield, provided that $M_c(I) > 1.0$, i.e., a supersonic crossflow point. The parameter ΔM_c in Eq. (7) is an arbitrary, user-defined constant. The purpose of this constant is to allow small compressions to occur without a penalty. Thus, if the drop in crossflow Mach number is less than or equal to ΔM_c, then the constraint is not violated. This constraint could also have been formulated on surface pressure gradient as a means of preventing flow separation.

At each analysis call, a composite airfoil consisting of a linear combination of n basis airfoils is evaluated. The composite airfoil for evaluation is defined by

$$\bar{Y} = a_i Y_i', \qquad i = 1, n \tag{8}$$

where Y_i' are user-specified basis airfoils and the a_i are the weighting factors that are the design variables $\bar{X}$. The angle of attack can be a design variable or a user-specified design constant. The basis airfoils are analytically defined and were chosen based on previous favorable experience with a high-lift cambered wing that was designed using NCOREL and experimentally verified[19] at $M = 1.62$. The airfoils chosen as basis airfoils have the modified NACA four-digit thickness distribution and circular arc camber surfaces. The modified NACA four-digit thickness distribution allows control of the maximum thickness ratio, maximum thickness location, and leading-edge radius. The circular arc camber allows control of the wing tip camber angles and also has a relatively flat camber surface inboard that is important for practical application.

The design constants are Mach number, leading-edge sweep angle, maximum thickness ratio, and maximum thickness loca-

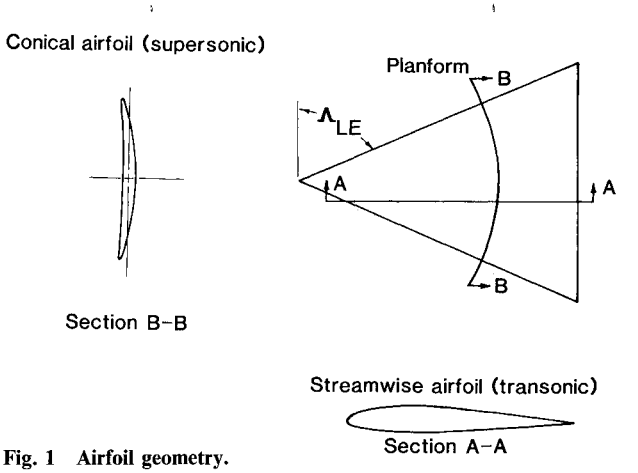

Fig. 1 Airfoil geometry.

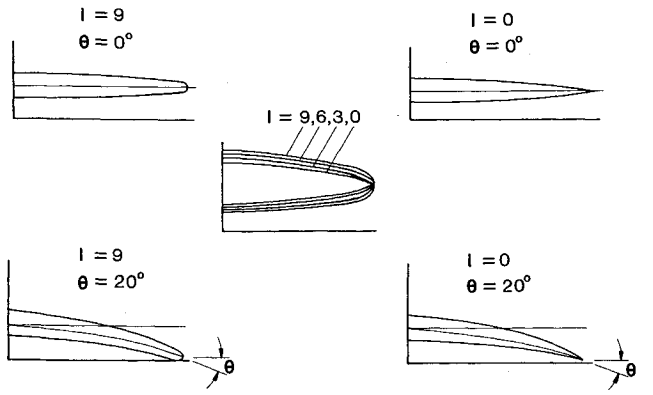

Fig. 2 Example basis airfoils, NACA 0004-14 thickness circular arc chamber.

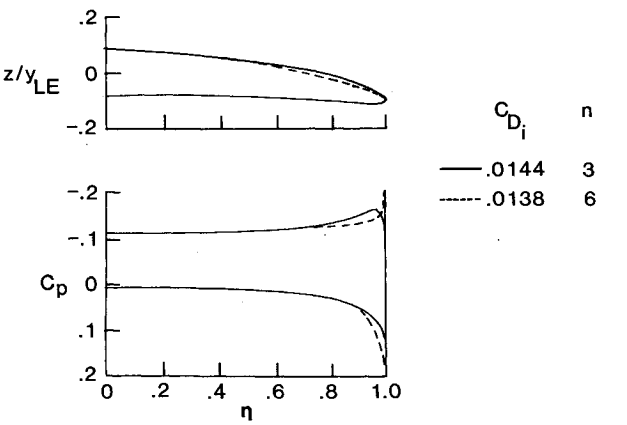

Fig. 3 Effect of different basis on the optimum airfoil, M = 1.60, α = 4 deg, Λ_{LE} = 60 deg, $C_{L_{design}}$ = 0.150.

tion. The number of basis airfoils does not change as the optimization process advances, but the user initially specifies the number of basis airfoils as well as the exact shape of each basis airfoil by setting the leading-edge-radius parameter I and the wing tip camber angle θ. Some example basis airfoils are shown in Fig. 2. The thickness distribution is specified as a NACA 0004-I4 thickness where I is the integer leading-edge radius parameter that varies from 0 (sharp leading edge) to 9 (rounded leading edge). The inset in Fig. 2 better illustrates the effect of varying I on the leading-edge radius. The camber surface is specified by the wing tip camber angle that varies from 0 deg (flat wing) to some large value, e.g., 40 or 50 deg. However, large camber angles should be avoided in basis airfoils because a sufficiently large camber angle can move the stagnation point to the upper surface of the wing at a low angle of attack, effectively making the upper surface of the wing the lower surface to the airflow. This flow condition will slow convergence of the aerodynamic code.

Optimization Strategy

The way that NCOREL and CONMIN are coupled has an influence on the computational efficiency of the optimization procedure. The most direct method is to call NCOREL for each perturbation of the design variables and then allow CONMIN to use the aerodynamic information to move in the design space toward the minimum. However, this approach is costly and several means of reducing computational time were studied. The approaches taken to reduce execution time focused entirely on the NCOREL code, since most of the computational work occurs there.

Two test cases at $M = 1.60$ and $\alpha = 4$ deg are chosen as model problems to define an efficient optimization strategy. The specified lift coefficient is $C_{L_{design}} = 0.150$ and the angle of attack is a design constant rather than a design variable for these two model problems. A summary of pertinent information is listed in Table 1. The first model problem consists of three basis airfoils ($n = 3$) defined in Table 1. Twelve NCOREL calls were required for an execution time of 11.4 min on the CDC CYBER 175 computer. The second model problem consists of six basis airfoils ($n = 6$). This problem required 26 NCOREL calls and 24.5 min of CYBER 175 time. The original execution of the optimization procedure (labeled control in Table 1) initiated each aerodynamic analysis from freestream conditions. The column labeled Restart indicates that the converged aerodynamic solution from an aerodynamic analysis is saved and used to initiate the aerodynamic analysis of the next airfoil. The restart procedure basically provides an improved starting solution for each airfoil except for the first, which still must start from freestream conditions. The result of this approach is a reduction in execution time of 63 and 81% for the $n = 3$ and 6 cases, respectively. A further reduction in execution time is realized by using the AFIZ solver[15] instead of the SLOR solver.[12] The AFIZ scheme yielded a 36 and 11% reduction in run times compared to SLOR for the $n = 3$ and 6 cases, respectively (the restart option is still used). Further improvement was achieved by utilizing a CDC VPS-32 parallel-processing computer. Although the NCOREL code is not presently vectorized for the VPS-32, significant reductions in execution time are shown. The $n = 3$ model problem yielded a further 63% reduction and the $n = 6$ case a 54% reduction. Overall, the total reduction in execution time from the original procedure (control) to the final VPS-32 time is 91 and 92% for the $n = 3$ and 6 cases, respectively. Further improvements in computer resource requirements can be expected through grid refinement, vectorization of the NCOREL code for the VPS-32 processor, and approximate optimization strategies (e.g., Ref. 20). However, the most efficient optimization strategy shown in Table 1 was selected as the approach for the remainder of the

Table 1 Timing study of optimization procedure

No. of basis airfoils n	Basis airfoil description I θ, deg	Initial weights	NCOREL calls	CDC CYBER 175, CPU min Control	Restart	AFIZ	VPS-32 computer
3	9 0	1.0	12	11.4	4.2	2.7	1.0
	3 0	0.5					
	0 40	0.5					
6	9 0	1.0	26	24.5	4.6	4.1	1.9
	3 0	0.5					
	0 0	0.5					
	3 10	0.5					
	3 20	0.0					
	0 30	0.0					

research. Finally, a 29 × 19 computational grid was selected to achieve a further 16% reduction in run time compared to the 29 × 29 grid.

All the optimization strategies discussed in this section of the paper converged to the same optimum airfoil and flowfield to the fourth decimal place. Also, several of the intermediate airfoils that were defined by the optimizer were randomly selected for separate analysis by the NCOREL code. Each airfoil analyzed separately in the NCOREL code yielded the same flowfield as determined in the optimization procedure for that same airfoil. This indicates that the choice of the starting solution for the aerodynamic code (i.e., starting from the freestream condition or a previously obtained solution on a similar airfoil) does not influence the final result of each aerodynamic calculation.

Optimization Results

Fixed α

Example results are now presented for several cases in which the angle of attack is treated as a design constant. The optimum airfoils and the corresponding optimum pressure distribution for the two model problems previously discussed are shown in Fig. 3. The design constants are Mach 1.60, 4-deg angle of attack, and 60-deg leading-edge sweep angle. The design lift coefficient is 0.15. The variable in Fig. 3 is n, the number of basis airfoils. The difference between the $n = 3$ and 6 optimum airfoils is confined to the upper surface outboard of about 60% of the semispan. The $n = 6$ airfoil has a thinner section in this region compared to the $n = 3$ airfoil and, consequently, also has a lower inviscid drag coefficient. The corresponding pressure distributions differ on both the lower and upper surface in the leading-edge region due to a slight shift in the stagnation point. More important, the character of the two pressure distributions is different, i.e., the $n = 6$ pressure distribution exhibits a small leading-edge suction spike that is undesirable because such spikes are intuitively linked to flow separation. However, the presence of the leading-edge suction spike is sometimes grid related in that it disappears on a finer grid. To examine the grid effects, an NCOREL analysis of the $n = 6$ optimum airfoil was performed on a 57 × 37 grid and the leading-edge suction spike remained on this fine grid, although the peak was reduced. This result indicates that the $n = 6$ airfoil may experience some leading-edge flow separation in the viscous flow. Since the inviscid drag coefficient is lower for this airfoil, an objective function based solely on the inviscid drag coefficient without a constraint on the pressure gradient or crossflow Mach number gradient may not always provide the best optimum in the viscous flow. However, it is possible to avoid this problem to some extent by choosing basis airfoils that do not overly emphasize a sharp leading edge. This is shown by the $n = 3$ optimum airfoil and its corresponding pressure distribution, which does not have a leading-edge suction spike.

The set of basis airfoils used for further study are defined in Table 2. These basis airfoils were chosen to provide a broad range of I and θ. The design constants stated in the beginning of this section were chosen as the baseline. Various perturbations about the baseline are now considered.

The first perturbation considered is on $C_{L_{design}}$. The result of an optimization for $C_{L_{design}}$ values of 0.165, 0.150, and 0.125 at a constant $\alpha = 4$ deg is presented in Fig. 4. The airfoils resulting from the optimization vary considerably, as do the pressure distributions corresponding to those airfoils. The optimum airfoils show that camber is used to relieve the pressures and thereby reduce the lift coefficient at constant angle of attack. The $C_{L_{design}} = 0.150$ pressure distribution is seen to be free of the leading-edge pressure spike that was previously noted for the $n = 6$ case for the same conditions. However, this phenomenon does develop as the lift coefficient is increased to 0.165. Also shown in Fig. 4 is the crossfow Mach number distribution corresponding to the optimum airfoils. The crossflow Mach number is a two-dimensional Mach number that ignores the radial component of the velocity vector and so

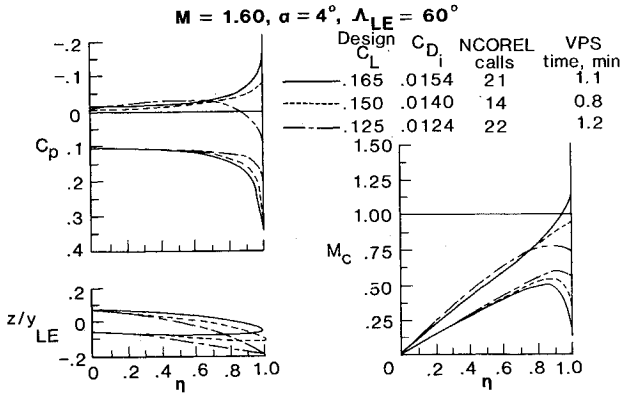

Fig. 4 Effect of $C_{L_{design}}$ at constant α on the optimum airfoil.

Table 2 Set of basis airfoils

I	θ, deg	I	θ, deg
9	0	3	10
3	0	3	30

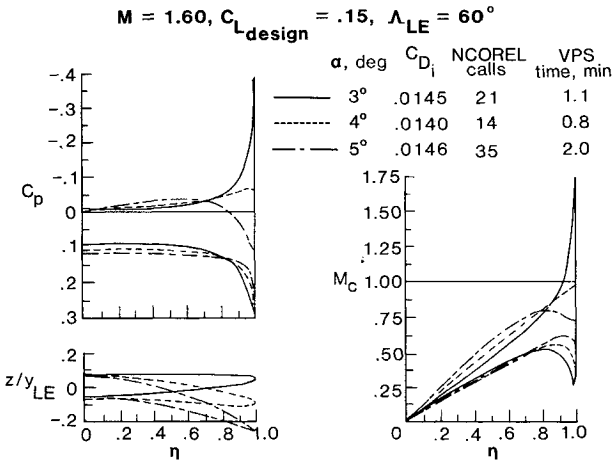

Fig. 5 Effect of α at constant $C_{L_{design}}$ on the optimum airfoil.

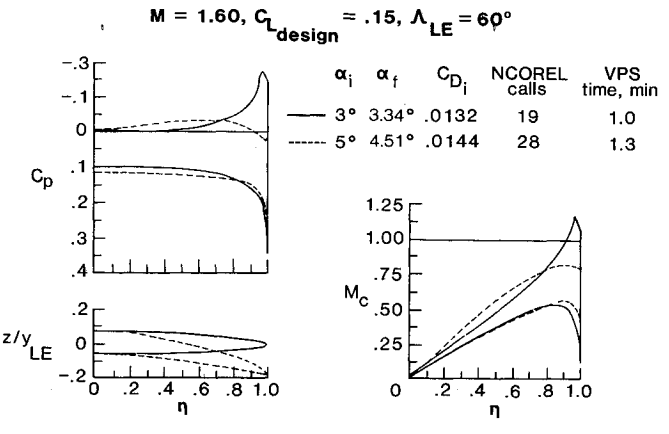

Fig. 6 Effect of initial α on the optimum airfoil where α is a design variable.

is analogous to the local transonic (two-dimensional) Mach number discussed in the analysis of transonic airfoils. The crossflow Mach numbers are subsonic for the $C_{L_{design}} = 0.125$ and 0.150 cases, but there is a small supersonic crossflow region for the $C_{L_{design}} = 0.165$ case. This region corresponds to the leading-edge suction spike noted in the pressure distribution for that airfoil. Therefore, the leading-edge suction spike is a rapid expansion to supersonic crossflow conditions that is almost immediately followed by a crossflow shock. For a sufficiently strong crossflow shock at the leading edge, boundary-layer separation may result in viscous flow.

An angle-of-attack variation at constant $C_{L_{design}}$ is shown in Fig. 5. Once again, considerable variation occurs in the optimum airfoils and corresponding pressure distributions. The results can be impractical, as illustrated by the $\alpha = 3$-deg case. The pressure distribution for this particular case is characterized by a leading-edge suction spike that is also clearly evident on the crossflow Mach number plot.

Variable α

The results of the previous section indicate that the angle of attack should also be considered as a design variable in addition to the weighting factors of the basis airfoils. The addition of a new degree of freedom should yield a better design, since the optimization procedure can now vary the airfoil thickness, camber, and angle of attack to find the best minimum drag design.

An optimum airfoil was determined for a $C_{L_{design}} = 0.150$ at $M = 1.60$. The four basis airfoils from the previous section are utilized and the design variables are the four weighting factors plus angle of attack. Several different initial angles of attack were selected to start the optimization process. The optimum airfoils for the initial angles of attack of 3 and 5 deg are presented in Fig. 6, along with the corresponding pressure and crossflow Mach number distributions. The difference between the two optimum airfoils is significant. The final angle of attack of the optimum airfoil for which the initial angle of attack was 3 deg is 3.34 deg. The final angle of attack of the optimum airfoil for which the initial angle of attack was 5 deg is 4.51 deg. The first airfoil represents a minimum drag airfoil that relies primarily on flat plate lift, whereas the second airfoil uses camber to relieve the flat-plate lift of the higher initial angle of attack. The result of this analysis indicates that the design space possesses local minima in addition to those shown previously for different basis airfoils. Also, the pressure distributions for both airfoils are less than desirable because of the rapid expansion at the leading edge. The more cambered airfoil exhibits a small leading-edge suction spike, but the spike does not become supersonic.

One means of determining the best solution from a number of candidate optimum airfoils designed for the same conditions might be found in the inviscid drag polar. The inviscid drag polar for the two airfoils of Fig. 6 is given in Fig. 7. The more cambered airfoil has a higher inviscid drag coefficient at $C_{L_{design}}$, but for lift coefficients more representative of maneuver conditions, e.g., $C_L = 0.40$, the more cambered airfoil is superior.

Another method for dealing with leading-edge pressure spikes or a larger region of supersonic crossflow is the addition of a constraint on the crossflow Mach number gradient. A

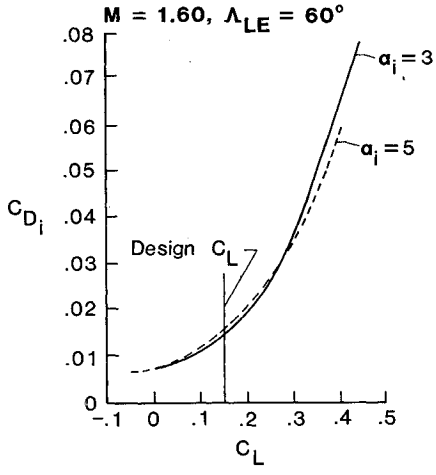

Fig. 7 Drag polar for two optimum airfoils designed for the same conditions.

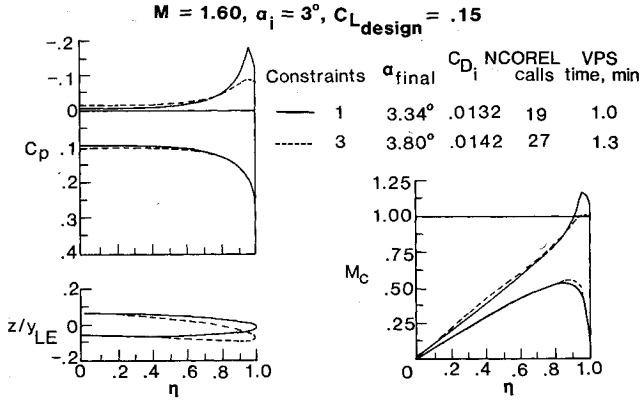

Fig. 8 Effect of the crossflow Mach number gradient constraint when α is a design variable.

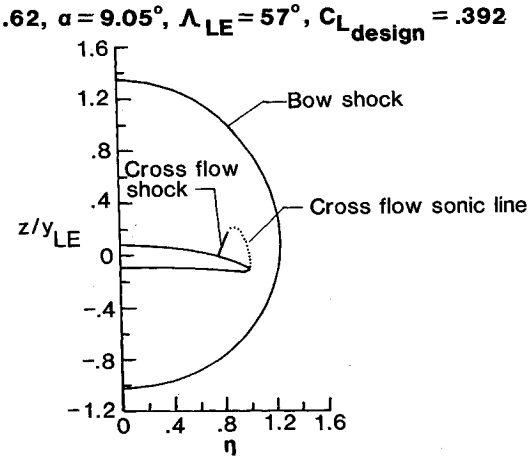

Fig. 9 High α flowfield description.

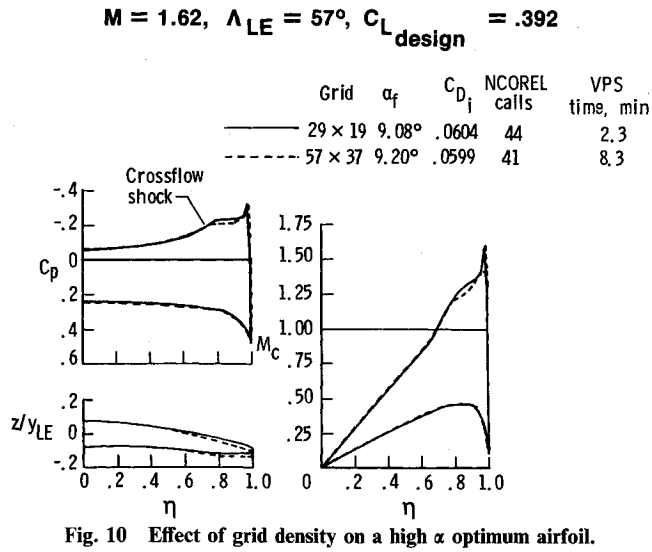

Fig. 10 Effect of grid density on a high α optimum airfoil.

constraint of the form of Eq. (7) was added with $\Delta M_c = 0.15$ and the variable-angle-of-attack case with an initial $\alpha = 3$ deg was re-examined. The results given in Fig. 8 show that angle of attack and camber are both used to satisfy the constraint on the crossflow Mach number gradient and that the optimum pressure distribution is improved by the addition of the crossflow Mach number gradient constraint. The final α for the original problem was 3.34 deg, whereas the additional constraint caused the final α to change to 3.80 deg. This additional constraint required additional analysis calls and computational time.

High α

The previous test cases focused on low-angle-of-attack conditions. Under these conditions, the flowfield is usually attached to the wing surface. A more difficult problem occurs for high angles of attack where flow separation is likely. One approach to the high-angle-of-attack problem is to use the wing camber and leading-edge radius to prevent flow separation at a high angle of attack. This attached flow approach to high-angle-of-attack flows was experimentally verified and reported in Ref. 19.

The essential features of the high-angle-of-attack, attached flow are shown in Fig. 9. The airfoil geometry, bow shock, crossflow shock, and crossflow sonic line are shown in this figure. The crossflow inside the bow shock (but outside the crossflow sonic line) is subsonic. At high angles of attack, the flow expands around the leading edge to supercritical crossflow Mach numbers, which is the region inside the crossflow sonic line. However, this flow must compress to subcritical crossflow. The recompression occurs through the crossflow shock, the location of which corresponds to the inboard portion of the crossflow sonic line.

The conditions for the high α problem are $M = 1.62$, $C_{L_{design}} = 0.392$, a leading-edge sweep angle of 57 deg, and a maximum thickness ratio of 5%. The design variable vector consists of the weighting factors of the composite airfoil and an angle of attack initially set to 9.6 deg. The lift constraints and crossflow Mach number gradient are applied with $\Delta M_c = 0.23$.

Optimum airfoils for the given high α conditions are presented for two different grid densities in Fig. 10. The finer 57×37 grid has approximately four times the grid density of the 29×19 grid. These two grid densities are illustrated in Fig. 11. The nondimensionalized optimum airfoils determined by the optimization procedure are shown in Fig. 10, along with the corresponding pressure and crossflow Mach number distributions. The airfoil resulting from the 57×37 grid is more cambered, but the lower surface pressure distributions are virtually identical for both grid densities. This is because the final α is 9.20 deg for the 57×37 grid, but 9.08 deg for the 29×19 grid. The differences between the two optimum pressure distributions are confined to the supercritical crossflow region on the upper surface. The pressure plateau is lower and the crossflow shock is somewhat weaker for the 57×37 grid compared to the 29×19 grid result, but the crossflow shock location is unchanged.

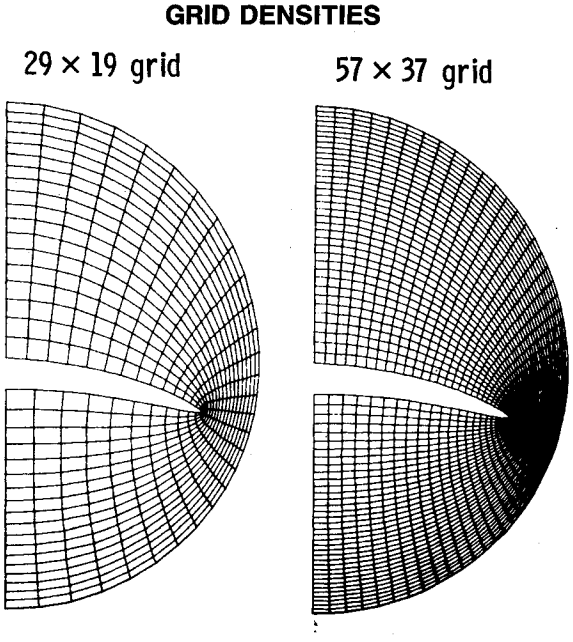

Fig. 11 Grids for aerodynamic solution.

A leading-edge suction spike of the same magnitude is found for both grid densities. In some instances, it was found that the finer grid significantly reduced or even eliminated the leading-edge suction spike. However, a leading-edge suction spike of some magnitude is generally present for the high α cases. The importance of this phenomenon was briefly discussed in the previous discussion for fixed α cases. The concern is that the leading-edge suction spike may represent a small leading-edge shock which might separate the real flow. Due to the irrotational and inviscid assumptions of the full-potential theory, flow separation cannot be predicted except through empirical shock strength conditions compared with experimental data. On the other hand, the leading-edge suction spike may occur due to insufficient grid resolution at the leading edge and, consequently, might disappear at some unknown grid density. From a numerical standpoint, leading-edge suction spikes slow numerical convergence and can cause solution divergence.

An example of controlling the supercritical crossflow region through the use of the crossflow Mach number gradient constraint is given in Fig. 12. Both results presented in this figure are for identical cases on a 29×19 grid and for values of $\Delta M_c = 0.23$ and 0.15. The optimizer utilized the outboard camber to reduce the leading-edge suction spike and the pressure plateau in the supercritical region. A higher angle of attack was chosen, with the result that the lower surface pressure distributions are virtually identical for both airfoils. The same positioning of the crossflow shock for the cases shown in Figs. 10 and 12 may indicate that the form of the basis airfoils does not allow control of the crossflow shock strength or position.

The results of high α airfoil optimization for several Mach numbers on a 29×19 grid are presented in Fig. 13. The initial conditions and the optimization criteria are the same for all three Mach number cases shown in Fig. 13. A nearly identical optimum lower surface pressure distribution is achieved for all three Mach numbers. This result is obtained through differing amounts of camber and final α for the several Mach numbers. However, the supercritical region on the upper surface is appreciably different for all three airfoils. The leading-edge suction spike occurs for all Mach numbers, but the peak pressure coefficient decreases for increasing Mach number. However,

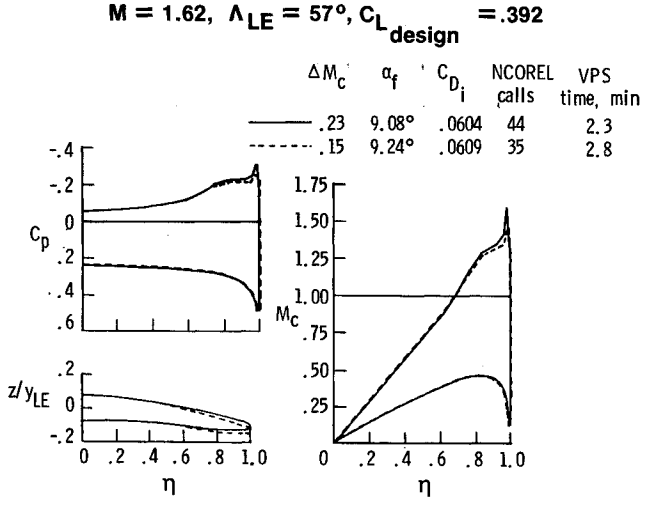

Fig. 12 Comparison of the effect of ΔM_c on optimum airfoils for the high α case and a 29×19 grid.

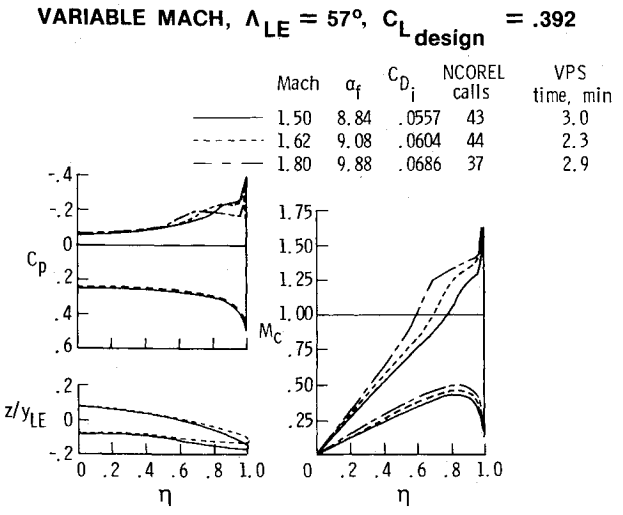

Fig. 13 High α optimum airfoils for several Mach numbers on a 29 × 19 grid.

the peak crossflow Mach number is nearly constant. The width of the supercritical region increases with increasing Mach number, but the pressure inboard of the crossflow shock is nearly independent of the freestream Mach number. The SLOR algorithm was used for the $M = 1.80$ case due to the difficulty of applying the AFIZ scheme for this nearly sonic leading-edge condition, i.e., $\beta\cot\Lambda_{LE} = 0.97$ for this case.

The number of analysis calls required to find the optimum is very important to the overall design process. A general criterion of $10 \times (n + 3)$ is presented without explanation in Ref. 20. This study has found that the number of analysis calls is generally $2\text{–}6 \times (n + 3)$. The reasons for the rather large difference between the number of analysis calls required for this study and the criterion stated in Ref. 20 are not known, but they are probably related to the analysis code itself, the flow regime, the choice of basis airfoils, and the formation of the constraints among other possible reasons.

Conclusion

A procedure for the optimization of supersonic airfoils has been developed. The procedure combines the NCOREL nonlinear, full-potential aerodynamic code with the CONMIN numerical optimizer. The airfoils analyzed in the NCOREL code are formed by a linear combination of user-specified basis airfoils. The weighting factors of the basis airfoils form the design variable vector. The angle of attack can be a design constant or a design variable. The inviscid drag coefficient is minimized subject to lift coefficient and crossflow Mach number gradient constraints.

The linking of the aerodynamic code and the optimization algorithm has a strong influence on the computational efficiency. Several straightforward means of reducing computational time were investigated and a reduction of 90% in execution time was shown compared to the original procedure.

Test cases for a constant angle of attack showed that the procedure can produce an impractical airfoil for certain combinations of the user-specified lift coefficient and angle of attack. These cases also showed that the final optimum airfoil is dependent on the initial user-specified basis airfoils. The angle of attack was subsequently included in the design variable vector and the final optimum was a function of the initial angle of attack. Several of the low-angle-of-attack test cases developed upper-surface regions of supercritical crossflow referred to as leading-edge suction spikes. These leading-edge suction spikes may be related to flow separation at the leading edge. A crossflow Mach number constraint was added that alleviated supercritical crossflow for a low-angle-of-attack case. This constraint also influenced the final angle of attack if this parameter was used as a design variable.

High-angle-of-attack test cases revealed the presence of a crossflow shock in addition to the leading-edge suction spikes. Increased grid density did not appreciably change the result of the optimization process, with the exception of the execution time. Several Mach numbers were investigated at high α to show the robustness of the procedure, including a nearly sonic leading-edge condition.

This two-dimensional study represents the first step in a process that will lead to a fully three-dimensional aerodynamic optimizer for wings in supersonic, inviscid flow. Structural deflections can be significant under high loadings and the possibility of incorporating structure deflections into the optimization will be investigated.

References

[1]Ashley, H., "On Making Things Best—Aeronautical Uses of Optimization," *Journal of Aircraft*, Vol. 19, Jan. 1982, pp. 5–28.

[2]Hicks, R. M., "Transonic Wing Design Using Potential Flow Codes—Successes and Failures," SAE Paper 810565, April 1981.

[3]Aidala, P. V., Davis, W. H. Jr., and Mason, W. H., "Smart Aerodynamic Optimization," AIAA Paper 83-1863, July 1983.

[4]Kennelly, R. A. Jr., "Improved Method for Transonic Airfoil Design-By-Optimization, AIAA Paper 83-1864, July 1983.

[5]Barris, C. B., Haney, H. P., and Sankar, N. N., "Computational Aerodynamic Design Methodology," AIAA Paper 83-1865, July 1983.

[6]Misegades, K. P., "Airfoil Optimization," AIAA Paper 84-0053, Jan. 1984.

[7]Cosentino, G. B. and Holst, T. L., "Numerical Optimization Design of Advanced Transport Wing Configurations," AIAA Paper 85-0424, Jan. 1985.

[8]Middleton, W. D. and Lundry, J. L., "A System for Aerodynamic Design and Analysis of Supersonic Aircraft. Part I, General Description and Theoretical Development," NASA CR-3351, Dec. 1980.

[9]Woodward, F. A. et al., "A Method of Optimizing Camber Surfaces for Wing-Body Combinations at Supersonic Speeds—Theory and Application," Boeing Document D6-10741, Pt. I, 1965.

[10]Stevens, J. R., "A New Lifting Surface Approach to the Design of Supersonic Wings," *AFWAL Design Conference Proceedings*, Vol. 1, Feb. 1976.

[11]Mack, R., "Effects of Leading-Edge Sweep Angle and Design Lift Coefficient on Performance of a Modified Arrow Wing at a Design Mach Number of 2.6," NASA TN D-7753, Dec. 1974.

[12]Siclari, M. J., "The NCOREL Computer Program for 3D Nonlinear Supersonic Potential Flow Computations," NASA CR-3694, Aug. 1983.

[13]Siclari, M. J., "Supersonic Nonlinear Potential Flow Analysis—Interim Report," NASA CR-172456, Aug. 1984.

[14]Vanderplaats, G. N., "CONMIN—A FORTRAN Program for Constrained Function Minimization–User's Manual," NASA TM X-62282, Aug. 1973.

[15]Siclari, M. J., "Approximate Factorization Schemes for 3-D Nonlinear Supersonic Potential Flow," AIAA Paper 83-0376, Jan. 1983.

[16]Fletcher, R. and Reeves, C. M., "Function Minimization by Conjugate Gradients," *British Computer Journal*, Vol. 7, No. 2, 1964, pp. 149–154.

[17]Zoutendijk, G. G., *Methods of Feasible Directions*, Elsevier, Amsterdam, The Netherlands, 1960.

[18]Vanderplaats, G. N. and Moses, F., "Structural Optimization by Methods of Feasible Directions," *Journal of Computers and Structures*, Vol. 3, 1973, pp. 739–755.

[19]Pittman, J. L., Miller, D. S., and Mason, W. H., "Supersonic, Nonlinear, Attached-Flow Wing Design for High Lift with Experimental Validation," NASA TP-2336, Aug. 1984.

[20]Vanderplaats, G. N., "Efficient Algorithm for Numerical Airfoil Optimization," *Journal of Aircraft*, Vol. 16, Dec. 1979, pp. 842–847.